Supporting Information

Nanoporous Metal-Organic Framework-Based Ellipsoidal Nanoparticles for the Catalytic Electroreduction of CO_2

Jin-Han Guo, Xiao-Yu Zhang, Xiao-Yao Dao, and Wei-Yin Sun *

Coordination Chemistry Institute, State Key Laboratory of Coordination Chemistry, School of Chemistry and Chemical Engineering, Nanjing National Laboratory of Microstructures, Collaborative Innovation Center of Advanced Microstructures, Nanjing University, Nanjing 210023, China

Corresponding Author：sunwy@nju.edu.cn (W.-Y. Sun)

1. Instruments

Powder X-ray diffraction (PXRD) data were collected on a Bruker D8 Advance X-ray diffractometer with Cu Kα (λ = 1.5418 Å) radiation. All the gas adsorption isotherms were measured on a Micromeritics ASAP 2020 system by employing a standard volumetric technique up to saturated pressure. Prior to gas adsorption experiments, the samples were activated under a dynamic vacuum at 200 ºC for 6 hours. The N_2 adsorption isotherms were monitored at 77 K, while CO_2 adsorption isotherms were obtained at 273 and 298 K. The X-ray photoelectron spectroscopy (XPS) measurements were conducted by using an ESCALAB 250XI high-performance electron spectrometer using monochromated Al Kα radiation (hv = 1486.7 eV) as the excitation source. The content of Ni was quantified by an Agilent 7800 ICP-MS. SEM observations were performed on a Hitachi S-4800 field emission scanning electron microscope at an accelerating voltage of 5 kV. The transmission electron microscopy (TEM), high-resolution TEM and EDS mapping were acquired on JEOL JEM 2100F equipped with an energy dispersive X-ray spectrometer at 200kV accelerating voltage.

2. Principle Analysis

For CO_2 electroreduction to CO in basic aqueous solution, the cathode equation is:

$$CO_2 + H_2O + 2e^- \rightarrow CO + 2OH^-$$

applying the Nernst equation:

$$E = E^{\theta}_{CO_2/CO} + \frac{RT}{2F}\ln\frac{c_{CO_2}}{c_{CO}c_{OH^-}^2} \quad \text{(S1)}$$

E: Applied potential / V vs SHE

$E^{\theta}_{CO_2/CO}$: Equilibrium potential of CO_2/CO couple / V vs SHE

R: Gas constant / 8.314 J mol^{-1} K^{-1}

T: Calvin temperature / K

F: Faradic constant / 96485 C mol^{-1}

c_i: Concentration of species i / mol L^{-1}

As it can be deduced from the eq. S1, a higher concentration of CO_2 leads to higher operating potential, which is favorable for CO_2 reduction.

Also, we refer to classical Butler-Volmer law:

$$i = 2k_0FA\left\{\exp\left[\frac{-\alpha F}{RT}\left(E - E^{\theta}_{CO_2/CO}\right)\right]c_{CO_2} - \exp\left[\frac{(1-\alpha)F}{RT}\left(E - E^{\theta}_{CO_2/CO}\right)\right]c_{CO}c_{OH^-}^2\right\} \quad \text{(S2)}$$

i: Operating current / A

k_0: Rate constant of the CO_2 electroreduction reaction

A: Geometric area of the electrode / cm^2

α: Transfer coefficient of the reaction

Under the same operating potential, the concentration of CO and hydroxide are constants. Thus, a higher concentration of CO_2 also magnifies the current.

For onset potential and constant current densities measurements, the concentration of CO and hydroxide are constants as well, we obtain:

$$E = E^{\theta} + \frac{RT}{2F}\ln c_{CO_2} + C \quad \text{(S3)}$$

When differing CO_2 concentration, for instance, the CO_2 concentrations in Ni_{20}-N-C and Ni-AB, the difference of the applied potential under the same current densities should be:

$$\Delta E = \frac{RT}{2F} \ln \frac{c_{CO_2,20\%\ \mathrm{Ni-N-C}}}{c_{CO_2,20\%\ \mathrm{Ni-}AB}} \tag{S4}$$

Considering the Henry's law and applying the effective pressure of CO_2 in the catalyst measured under 298 K and 1 atm for both catalysts eq. S4:

$$\Delta E_{\mathrm{cathode}} = \frac{RT}{2F} \ln \frac{35}{2.9} = 0.032\mathrm{V} \tag{S5}$$

For 6 M KOH, the effect on the anode potential can be calculated as the following equation:

$$\Delta E_{\mathrm{anode}} = \frac{RT}{4F} \ln \frac{1}{6} = -0.0115\mathrm{V} \tag{S6}$$

3. Material Synthesis

1) Synthesis of Ni-AB

TPPNi 40 mg and acetylene black (AB) 160 mg were mixed with 50 ml CH_2Cl_2. The mixture was sonicated for 30 min, then the CH_2Cl_2 was slowly rotate evaporated to form a homogeneous adsorption distribution of TPPNi on AB.

The precursor was heated from the room temperature to 800 °C with a heating rate of 5 °C/min, then pyrolyzed at 800 ℃ for 2 hours in a N_2 atmosphere. Subsequently, the nickel particles involved in the resultant product was removed by heating the samples 1 M nitric acid solution for 24 h at 80 °C. The black samples were collected by centrifugation, washed three times with distilled water and ethanol, and dried under an infrared lamp. Then the resulting powders were pyrolyzed again under the N_2 atmosphere at 800 ℃ for 1 hour to obtain Ni-AB.

2) Catalytic ink preparation

15 mg of catalyst and 75 μl of 5 wt% Nafion 117 solution (for tests in 6 M KOH 150 μL Nafion solution were used) were introduced into the water–isopropanol solution with equal volumes of water and isopropanol to a total volume of 3 ml and sonicated for 1 h.

3) Preparation of the $FeNiO_x$ anode[1]

Nickel foam with 1.5 mm thickness was cut into a 9 cm^2 square. Sonicated in 6 M HCl for 30 min to clean the nickel oxides layer on the surface, rinsed by water and then sonicate again in ethanol before drying under an infrared lamp. The electrodeposition was carried out in a standard three-electrode cell with circulating cooling water, nickel foam was clamped by a Pt electrode holder as the working electrode, a platinum plate as the counter electrode and a saturated Ag/AgCl as the reference electrode. 100 ml of electrolyte contained 3 mM $Ni(NO_3)_2{\cdot}6H_2O$ and 3 mM $Fe(NO_3)_3{\cdot}9H_2O$. The electrodeposition was carried out potential statically at -1.0 V (vs Ag/AgCl) at 10 ℃ for 6 min. After deposition, the nickel foam was withdrawn from the electrolyte, rinsed with water, sonicated briefly in ethanol and dried under an infrared lamp.

4. Electrochemistry Calculation Formulas

Faradic efficiency of CO and H_2 were calculated by the following equation:

$$FE_i = \frac{z_i \times v \times C_i \times F}{V_M \times A \times j_{total}} \times 100\% \quad \text{(S7)}$$

FE_i: Faradaic efficiency of the product *i* / %

z_i: Charge transfer of product *i*

v: Gas flow rate of the out-flow from the flow chamber / L s^{-1}

C_i: Concentration of the product *i* detected by GC / Volume fraction

V_M: Molar volume of an ideal gas at 298 K / 24.45 L mol^{-1}

j_{total}: Total current density / A cm^{-2}

TON and TOF calculation

TOFs normalized to mass were calculated according to the following equation:

$$TOF_M = \frac{j_{total} \times FE_i \times M_{Ni}}{2F \times w_{icp-ms} \times \rho} \quad \text{(S8)}$$

TOF_M: Turnover frequency normalized to mass / s^{-1}

$w_{icp\text{-}ms}$: Weigh content of Ni in catalysts determined by ICP-MS / %

ρ: Catalysts loading density on the gas diffusion layer / g cm^{-2}

M_{Ni}: Molecular weight of nickel / 58.7 g mol^{-1}

TOFs normalized to ECSA were calculated by the following equation:

$$TOF_E = \frac{j_{total} \times FE_{CO} \times S_{Graphene} \times M_C}{2F \times ECSA \times w_{xps}} \quad \text{(S9)}$$

TOF_E: Turnover frequency normalized to electrochemical active surface area / s^{-1}

$S_{Graphene}$: Surface area of graphene / 2600 m^2 g^{-1}

M_C: Molar weight of carbon / 12 g mol^{-1}

$ECSA$: Electrochemical active surface area / m^2

w_{xps}: Atomic percentage of Ni at the surface of catalyst determined by XPS / %

Then TONs can be calculated by the following equation:

$$TON = \frac{C \times FE_{CO} \times S_{Graphene} \times M_C}{2F \times A \times ECSA \times w_{xps}} \quad \text{(S10)}$$

TON: Turnover number

C: Electric quantity / C

Cathode energy efficiencies are determined by:

$$CEE = \frac{1.34\text{V}}{1.23\text{V} - E_{cathode}} \times FE_{CO} \quad \text{(S11)}$$

CEE: Cathode energy efficiency / %

$E_{cathode}$: Applied potential on the cathode / V vs RHE

Full-cell energy efficiencies are calculated from the following equation:

$$EE = \frac{1.34\text{V}}{E_{\text{full-cell}}} \times FE_{CO} \quad \text{(S12)}$$

EE: Full-cell energy efficiency / %

$E_{\text{full-cell}}$: Applied potential on the cell / V

5. Computational Modelling

1) CO_2 solubility in electrolyte solutions[2, 3]

Presuming CO_2 in gas phase acts as an ideal gas, Henry's Law can be adopted to determine the solubility of CO_2 in pure water:

$$\left[CO_2\right]_{aq,0} = K_0 p_{CO_2,g} \tag{S13}$$

In which the coefficient, K_0, for CO_2 can be determined by a function of temperature:

$$\ln\left(K_0\right) = 93.4517 \times \left(100/T\right) - 60.2409 + 23.3585 \ln\left(T/100\right) \tag{S14}$$

However, in electrolytes the solubility of CO_2 is influenced by the salting-out effects, which can be described by the Sechenov equation:

$$\log\left(\left[CO_2\right]_{aq,0} / \left[CO_2\right]_{aq}\right) = K_s C_s \tag{S15}$$

Where K_s demonstrates the Sechenov constant and C_s is the concentration of the electrolyte solution. K_s is a function of specific ions in solution and the dissolved gas. The data can be found in the work conducted by Weisenberger et al,[2] and were listed in Table S1.

$$K_s = \sum\left(h_{ion} + h_G\right) \tag{S16}$$

$$h_G = h_{G,0} + h_T\left(T - 298\right) \tag{S17}$$

Table S1: Parameters for Sechenov constant in $KHCO_3$ and KOH solutions

Effects of Ions	
Ions	h_{ion}
K^+	0.092
HCO_3^-	0.097
OH^-	0.084
CO_2 Parameters	
$h_{G,0}$	-0.017
h_T	-0.00034

Thus, we obtain the solubilities of CO_2 in 0.5 M $KHCO_3$, 2 M $KHCO_3$ and 6 M KOH aqueous solutions are 0.0286, 0.0168 and 0.00483 mol L^{-1} at 298 K, respectively, revealing non-negligible differences compared with CO_2 solubility in pure water, which is 0.0342 mol L^{-1}.

2) Modeling of CO_2 reduction reaction in H-cell[4, 5]

In H-cell configuration, CO_2 is delivered by the bulk electrolyte with stirring. It is generally accepted that the bulk electrolyte is saturated with CO_2. With CO_2 consumed on the electrode, the CO_2 in bulk electrolytes will diffuse to the electrode due to the concentration gradient, and finally reaches an equilibrium. However, due to fluid boundary layers, the supplement of CO_2 is limited by the diffusion process, resulting in lower CO_2 concentration on the electrode compared with the bulk solution. When the CO_2 consumption rate reaches a specific value, the concentration on the electrode can be reduced to 0, leading to a limit current density value for CO_2 reduction. The maximum CO_2 reduction currents can be determined by the thickness of the diffusion layer and the type of electrolyte employed (Figure S1). With higher stirring speed, the diffusion layer thickness could be reduced, leading to higher CO_2 concentration on the electrode to achieve higher current density.

Equilibrium reactions in the CO_2-$KHCO_3$ electrolyte system in alkaline solution at 298 K and the diffusion coefficients of each species are:[3]

$$CO_2 + OH^- \underset{k_{1r}}{\overset{k_{1f}}{\rightleftharpoons}} HCO_3^- \qquad K_1 = 1.3\times10^8 \ \ M^{-1}$$

$$HCO_3^- + OH^- \underset{k_{2r}}{\overset{k_{2f}}{\rightleftharpoons}} CO_3^{2-} + H_2O \qquad K_2 = 8.5\times10^4 \ \ M^{-1}$$

$k_{1f} = 2.23\times10^{3}\ \mathrm{M^{-1}\ s^{-1}}$

$k_{1r} = 1.72\times10^{-5}\ \mathrm{M^{-1}\ s^{-1}}$

$k_{2f} = 6\times10^{9}\ \mathrm{s^{-1}}$

$k_{2r} = 7.06\times10^{4}\ \mathrm{s^{-1}}$

$D_{CO_2} = 1.91\times10^{-9}\ \mathrm{m^2\ s^{-1}}$

$D_{HCO_3^-} = 9.23\times10^{-10}\mathrm{m^2\ s^{-1}}$

$D_{CO_3^{2-}} = 1.19\times10^{-9}\mathrm{m^2\ s^{-1}}$

$D_{OH^-} = 5.27\times10^{-9}\mathrm{m^2\ s^{-1}}$

To modeling the CO_2 reduction in H-cell, the diffusion layer thickness (δ) is varying between 10 μm and 100 μm. The diffusion layer is modeled with the following equations with MATLAB R2018b software package with pdepe function:

$$\frac{\partial[CO_2]}{\partial t} = D_{CO_2}\frac{\partial^2[CO_2]}{\partial t^2} - k_{1f}[CO_2][OH^-] + k_{1r}[HCO_3^-] \tag{S18}$$

$$\frac{\partial[HCO_3^-]}{\partial t} = D_{HCO_3^-}\frac{\partial^2[HCO_3^-]}{\partial t^2} + k_{1f}[CO_2][OH^-] - k_{1r}[HCO_3^-] - k_{2f}[HCO_3^-][OH^-] + k_{2r}[CO_3^{2-}] \tag{S19}$$

$$\frac{\partial[CO_3^{2-}]}{\partial t} = D_{CO_3^{2-}}\frac{\partial^2[CO_3^{2-}]}{\partial t^2} + k_{2f}[HCO_3^-][OH^-] - k_{2r}[CO_3^{2-}] \tag{S20}$$

$$\frac{\partial[OH^-]}{\partial t} = D_{OH^-}\frac{\partial^2[OH^-]}{\partial t^2} - k_{1f}[CO_2][OH^-] + k_{1r}[HCO_3^-] - k_{2f}[HCO_3^-][OH^-] + k_{2r}[CO_3^{2-}] \tag{S21}$$

The initial values of each species are their equilibrium values calculated by MATLAB R2018b software. At the left boundary (electrode), CO_2 is consumed and OH^- is formed in the electrolysis process and are described by the following equations:

$$D_{CO_2}\frac{\partial[CO_2]}{\partial x} = -\frac{jFE_{CO}}{2F} \tag{S22}$$

$$D_{OH^-}\frac{\partial[OH^-]}{\partial x} = \frac{j}{F} \tag{S23}$$

As in our experiments, FE_{CO} is almost 100%, for simplicity, we take FE_{CO} = 100% in the modeling for all the calculations. Other species at the left boundary are prescribed by zero flux conditions. At the right boundary (bulk solution), each species is described as its equilibrium value.

3) Modeling of CO_2 reduction reaction in flow-cell[5, 6]

In flow-cell, CO_2 is supplied from the gas phase beyond the left boundary of the

catalyst layer. The diffusion path to the catalyst is much shorter, which guarantees the higher CO_2 concentration in the catalyst layer, leading to a higher reduction current density limit.

Although the governing equations of the diffusion layer in flow-cell configuration is same with which in H-cell, the equations of the catalyst layer are different due to the consumption of CO_2 and formation of OH^- inside the layer, taking the porosity of the catalyst layer into account, the equations can be written as follow with new source terms in catalyst layer with the assumption that the reaction occurs homogeneously throughout the catalyst layer:

$$\frac{\partial[\mathrm{CO_2}]}{\partial t} = D_{CO_2}\frac{\partial^2[\mathrm{CO_2}]}{\partial t^2} - k_{1f}[\mathrm{CO_2}][\mathrm{OH^-}] + k_{1r}[\mathrm{HCO_3^-}] - r_{\mathrm{CO_2}} \tag{S24}$$

$$\frac{\partial[\mathrm{HCO_3^-}]}{\partial t} = D_{HCO_3^-}\frac{\partial^2[\mathrm{HCO_3^-}]}{\partial t^2} + k_{1f}[\mathrm{CO_2}][\mathrm{OH^-}] - k_{1r}[\mathrm{HCO_3^-}] - k_{2f}[\mathrm{HCO_3^-}][\mathrm{OH^-}] + k_{2r}[\mathrm{CO_3^{2-}}] \tag{S25}$$

$$\frac{\partial[\mathrm{CO_3^{2-}}]}{\partial t} = D_{CO_3^{2-}}\frac{\partial^2[\mathrm{CO_3^{2-}}]}{\partial t^2} + k_{2f}[\mathrm{HCO_3^-}][\mathrm{OH^-}] - k_{2r}[\mathrm{CO_3^{2-}}] \tag{S26}$$

$$\frac{\partial[\mathrm{OH^-}]}{\partial t} = D_{OH^-}\frac{\partial^2[\mathrm{OH^-}]}{\partial t^2} - k_{1f}[\mathrm{CO_2}][\mathrm{OH^-}] + k_{1r}[\mathrm{HCO_3^-}] - k_{2f}[\mathrm{HCO_3^-}][\mathrm{OH^-}] + k_{2r}[\mathrm{CO_3^{2-}}] + r_{OH^-} \tag{S27}$$

$$r_{\mathrm{CO_2}} = \begin{cases} -\dfrac{jFE_{CO}\varepsilon}{2FL_{cat}} & , \ 0 \le x \le L_{cat} \\ 0 & , \ x > L_{cat} \end{cases} \tag{S28}$$

$$r_{OH^-} = \begin{cases} \dfrac{j\varepsilon}{FL_{cat}} & , \ 0 \le x \le L_{cat} \\ 0 & , \ x > L_{cat} \end{cases} \tag{S29}$$

As in our experiments, FE_{CO} is almost 100%, for simplicity, we take FE_{CO} = 100% in the modeling for all the calculations. We assume the catalyst particles accumulate freely in the catalyst layer, which leads to a 40% porosity of the accumulation. In addition, according to the N_2 adsorption experiment at 77 K, the porosity of the catalyst is 61%, thus the porosity of the catalyst layer (ε) is assumed to be $40\% + 60\% \times 61\% = 77\%$. The thickness of the catalyst layer (L_{cat}) is around 200nm according to SEM images.

The initial values of each species are their equilibrium values (which are 0 for HCO_3^- and CO_3^{2-} in KOH electrolyte). At the left boundary, the concentration of CO_2

is fixed at its saturate concentration, while zero reflux conditions are applied to other species. At the right boundary, however, conditions have slight differences between $KHCO_3$ and KOH electrolyte. For $KHCO_3$ electrolyte, which can perform as a buffer, each species is described as its equilibrium value. Nevertheless, for KOH electrolytes, we apply zero flux conditions for CO_2, while other species are described by their equilibrium values.

6. DFT Simulation

Vienna ab initio simulation package (VASP)[7] was used to perform all the density functional theory (DFT) computations. The projector augmented wave (PAW)[8] pseudopotential was used for the core electrons, and a 480 eV cutoff energy for the valence electrons. The generalized gradient approximation (GGA) in the form of Perdew–Burke–Ernzerhof (PBE)[9] was employed for the exchange-correlation potentials.

The Ni-N-C catalyst was simulated using a (6 × 6) graphene sheet with Ni bonding to four N atoms in the double vacancy of graphene. A vacuum space of ~10 Å along the Z direction was used. A 3 × 3 × 1 Γ-centered k-mesh was used to sample the first Brillouin-zone with Gaussian smearing. The (100) crystalline facet of the pristine nickel was simulated by a 4 × 4 × 4 slab with a 10 Å vacuum along the Z-axis. To simulate the real bulk material and the surface, three bottom layers were fixed in their positions while the top layer was free to move due to interaction with the adsorbates. A 4 × 4 × 1 Γ-centered k-mesh was employed for the first Brillouin zone, with a first-order Methfessel-Paxton smearing parameter σ of 0.1 eV. The self-consistent field (SCF) convergence criterion is set to 1×10^{-4} eV for electronic iteration and the ionic relaxation continued until the maximum force was less than 0.02 eV $Å^{-1}$.

The Gibbs free energies were calculated at 298 K and 1 atm as outlined below:

$$G = H - T\Delta S = E_{DFT} + E_{ZPE} + \int_0^{298} C_V dT - T\Delta S \quad \text{(S30)}$$

G: Gibbs free energy / eV

H: Enthalpy / eV

S: Entropy / eV K^{-1}

E_{DFT}: Energy calculated by DFT / eV

E_{ZPE}: Vibrational zero-point energy / eV

C_V: Heat capacity at constant volume / eV K^{-1}

Gas-phase molecules were treated using the ideal gas approximation, whereas

adsorbates were treated using a harmonic approximation. The DFT-calculated energy for CO_2 was corrected by +0.45 eV,[6, 10] a usual adjustment to correct the overestimation by DFT. The relative free energies were calculated based on the computational hydrogen electrode (CHE) model.[10, 11] The details of calculation for energy diagram are listed in Table S2.

7. Q_{st} calculation[12]

The inflection characteristics of CO_2 adsorption isotherms necessitates the use of dual-site Langmuir model:

$$q = q_1 + q_2 = \frac{q_{sat,1} b_1 p}{1 + b_1 p} + \frac{q_{sat,2} b_2 p}{1 + b_2 p} \tag{S31}$$

where there are two distinct adsorption sites 1 and 2.

We can rewrite eq S31 as a quadratic polynomial of the pressures:

$$(q_{sat,1} + q_{sat,2} - q) b_1 b_2 p^2 + \left[\left(q_{sat,1} - q \right) b_1 + \left(q_{sat,2} - q \right) b_2 \right] p - q = 0 \tag{S32}$$

For any specified loading q, the corresponding pressure is obtained by solving the quadratic S33. If the temperature dependence of the two Langmuir constants b_1 and b_2 are described by

$$b_1 = b_{10} \exp\left(\frac{E_1}{RT} \right); b_2 = b_{20} \exp\left(\frac{E_2}{RT} \right) \tag{S33}$$

The isosteric heat of adsorption, Q_{st}, is defined as

$$Q_{st} = RT^2 \left(\frac{\partial \ln p}{\partial T} \right)_q \tag{S34}$$

where the derivative in the right member of eq S34 is determined at constant adsorbate loading, q. We can obtain the Q_{st} of each site from upper formulas.

b: adsorption coefficient / Pa^{-1}

E_i: the heat of adsorption of the site i / J mol^{-1}

p: bulk gas phase pressure / Pa

q: molar loading of adsorbate / mol kg^{-1}

q_{sat}: saturation loading / mol kg^{-1}

Q_{st}: isosteric heat of adsorption / J mol^{-1}

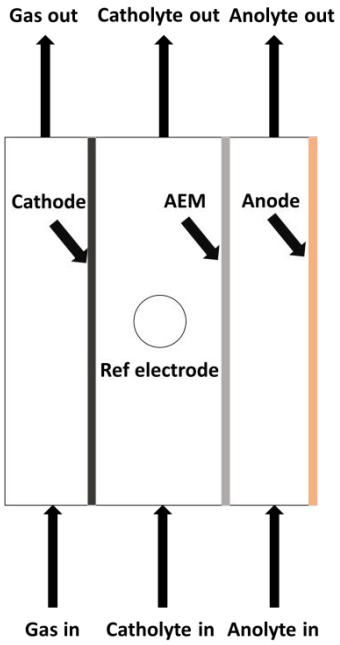

Figure S1. Schematic of the flow-cell used in our experiments

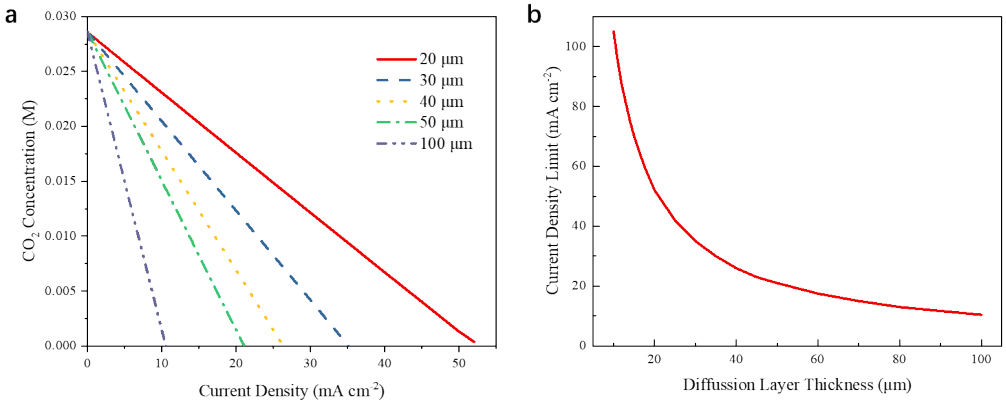

Figure S2. (a) CO_2 concentrations on the catalytic layer when operating with different current densities in the classic H-cell configuration with five diffusion layer thicknesses. (b) Current density limits and diffusion layer thickness relationship computed by the numerical solution of partial differential equations. All the data are calculated at 1 atm in 0.5 M $KHCO_3$ electrolyte, demonstrating that the current density for CDRR is limited due to inefficient supply of CO_2 in the electrolyte.[5, 13]

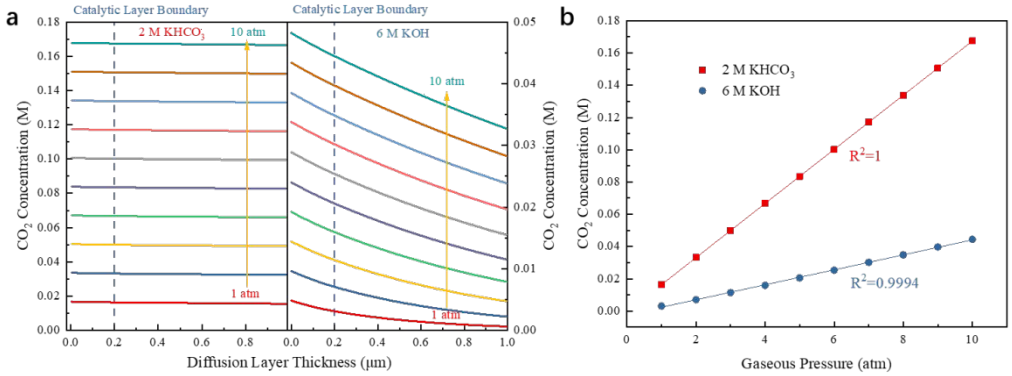

Figure S3. (a) CO_2 concentration distribution across the diffusion layer of the gas diffusion cell when applying 100 mA cm^{-2} current densities in 2 M $KHCO_3$ (left) and 6 M KOH (right) electrolytes at different gas pressures (also different gaseous concentration of CO_2) modeled by computation. (b) CO_2 concentrations at the catalytic layer boundaries of 2 M $KHCO_3$ and 6 M KOH electrolytes show the linear correlation to the concentrations in the gaseous phase. In gas-diffusion electrode (GDE) configuration,[5, 6, 14-17] CO_2 is supplied in the gaseous phase, securing its concentration in the catalytic layer of the electrode. The concentration of CO_2 of the three-phase interface on the electrode, where the reactions occur, is determined by Henry's Law.[2, 3] Indicating that augment the concentration of CO_2 in the gaseous phase also increases its concentration in the aqueous phase, leading to higher CDRR current densities and lower overpotentials.

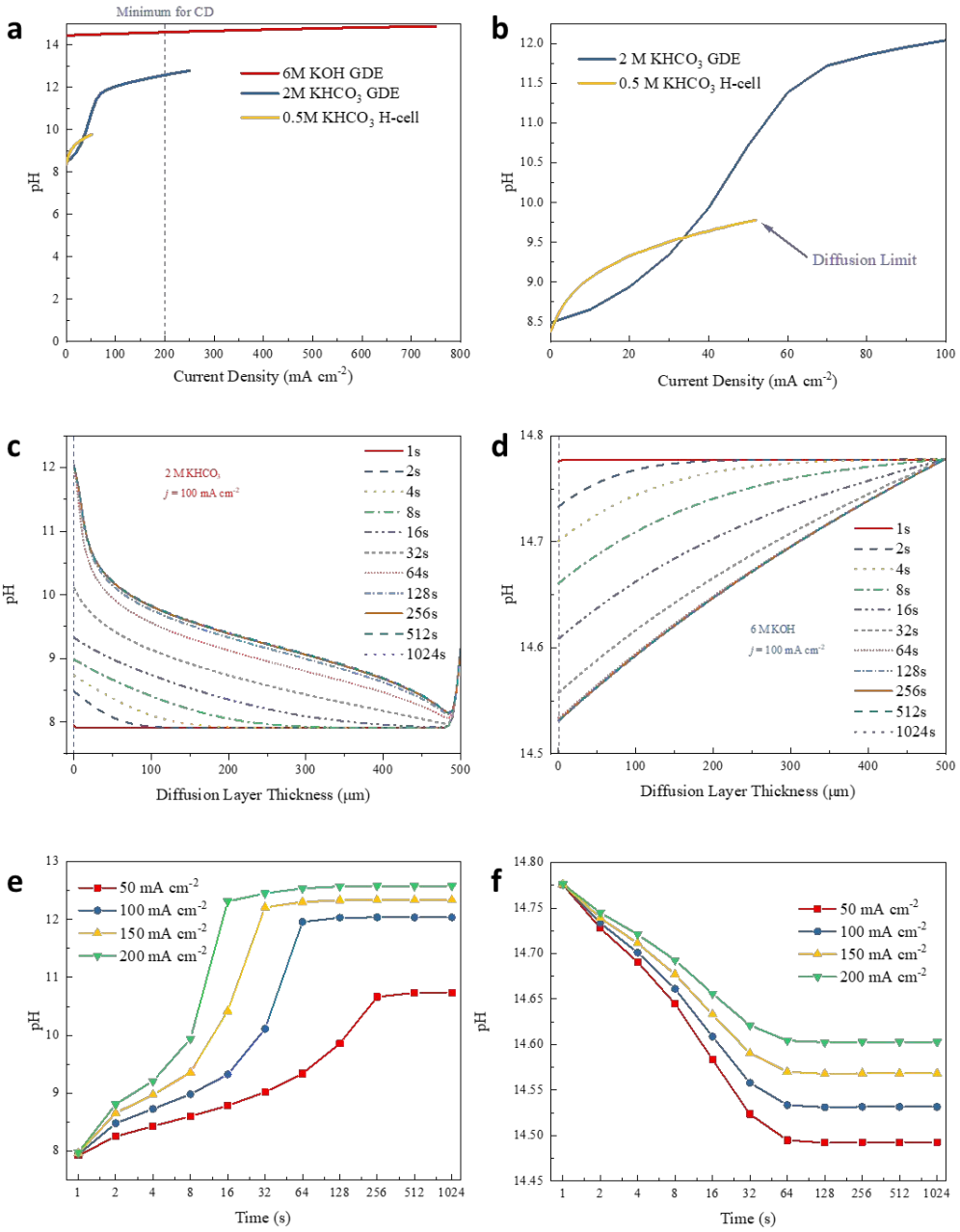

Figure S4. (a, b) Catalytic layer surface pH in different configurations at constant current density operation, the diffusion layer thickness for H-cell is assumed to be 20 μm. The pH distribution in diffusion layer of flow-cell at 100 mA cm^{-2} for 2 M $KHCO_3$ electrolyte (c) and 6 M KOH electrolyte (d). The time dependence of pH at the catalytic layer boundary (200 nm thickness) in flow-cells with 2 M $KHCO_3$ (e) and 6 M KOH electrolytes (f).

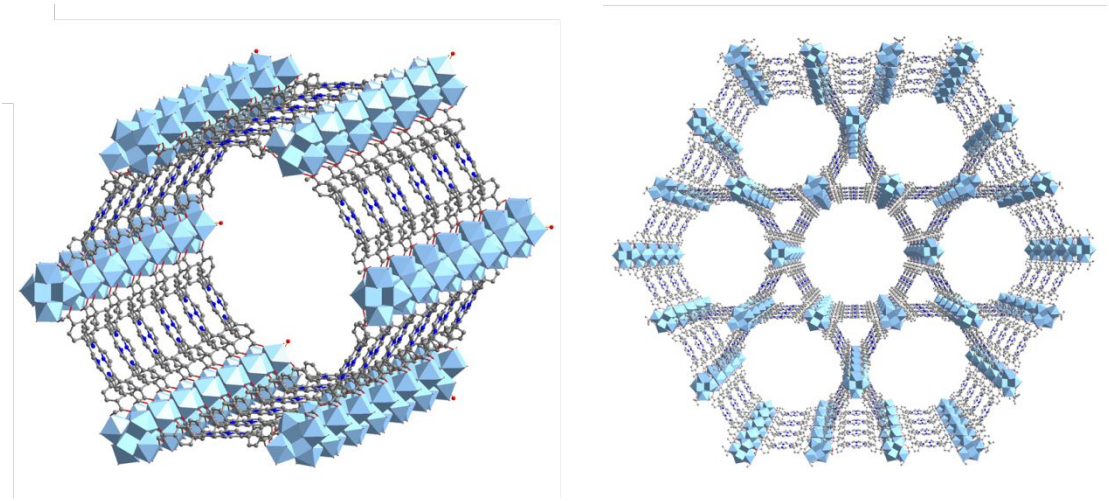

Figure S5. Structure of PCN-222, Zr-O cluster light blue polyhedron, C gray, O red, N blue.

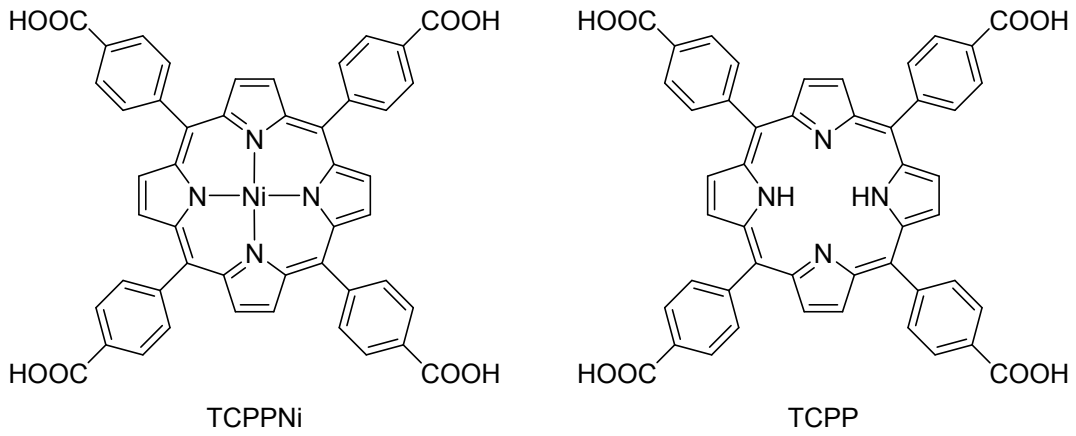

Figure S6. Porphyrin ligands utilized in the synthesis of the MOF precursors.

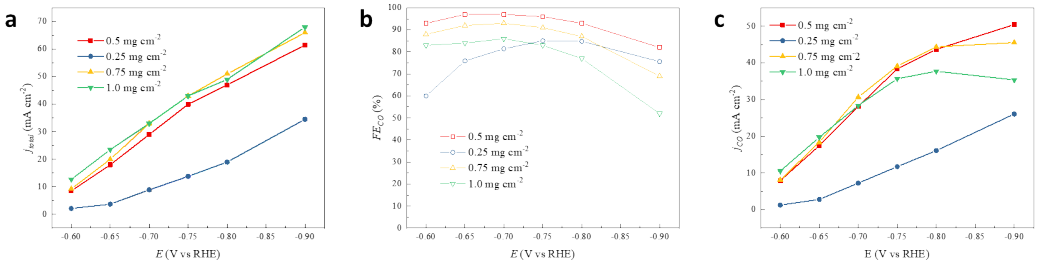

Figure S7. Effect of catalyst loading when utilizing Ni_{20}-N-C as the catalyst, it is clear that 0.5 mg cm^{-2} is optimum.

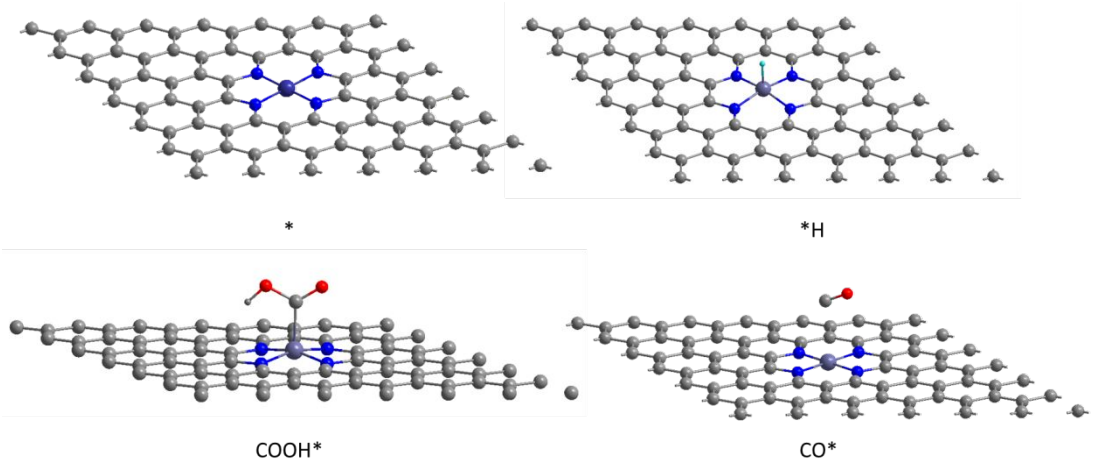

Figure S8. The optimized structures of the of intermediates on catalysts

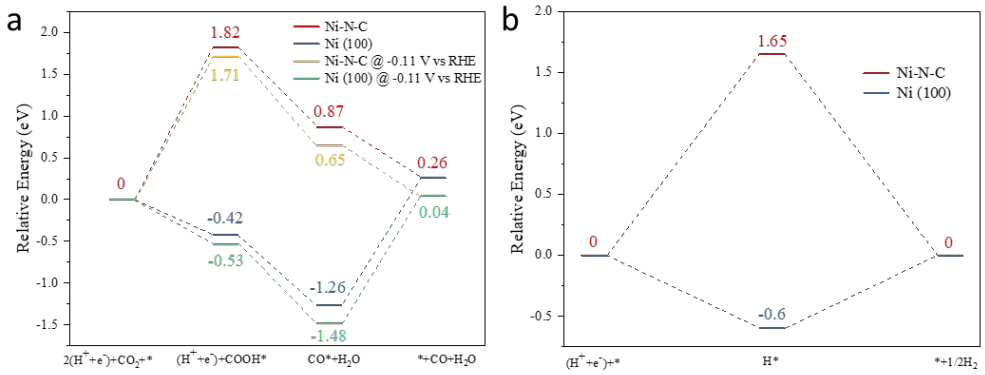

Figure S9. (a) Free energy diagram for the CO_2 reduction reaction to CO at E = 0 and -0.11 V vs RHE on Ni-N-C and Ni (100). (b) Free energy diagram for the H_2 evolution reaction at E = 0 V vs RHE on Ni-N-C and Ni (100). Based on DFT calculations.

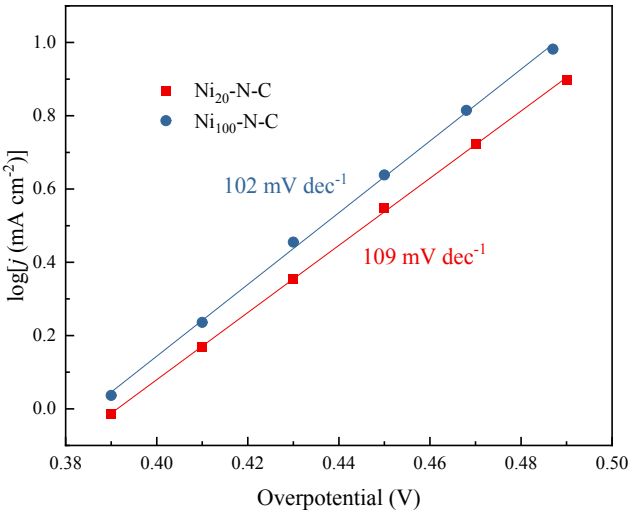

Figure S10. Tafel slope measurement of Ni_{20}-N-C and Ni_{100}-N-C in H-cell tests.

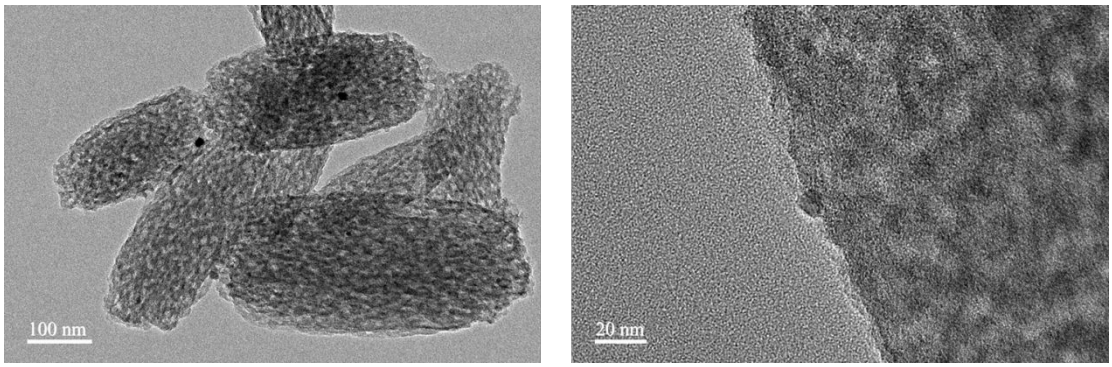

Figure S11. TEM images of Ni_{100}-N-C.

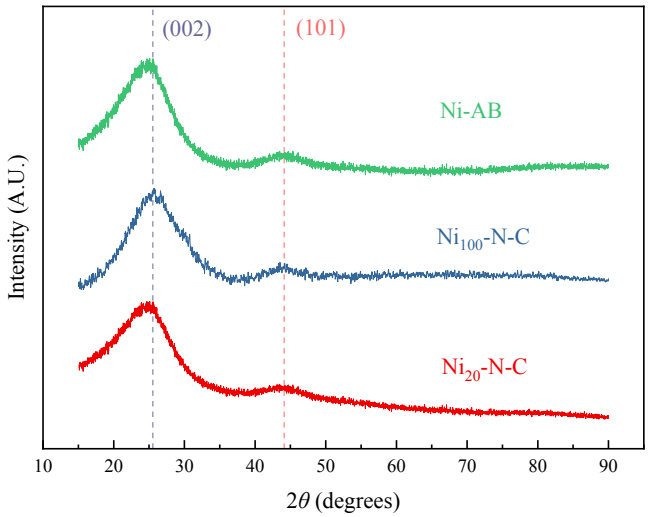

Figure S12. PXRD patterns of Ni_{20}-N-C, Ni_{100}-N-C, and Ni-AB. All demonstrate the (002) and (101) peaks of graphite, without detectable ZrO_2 and nickel particles.

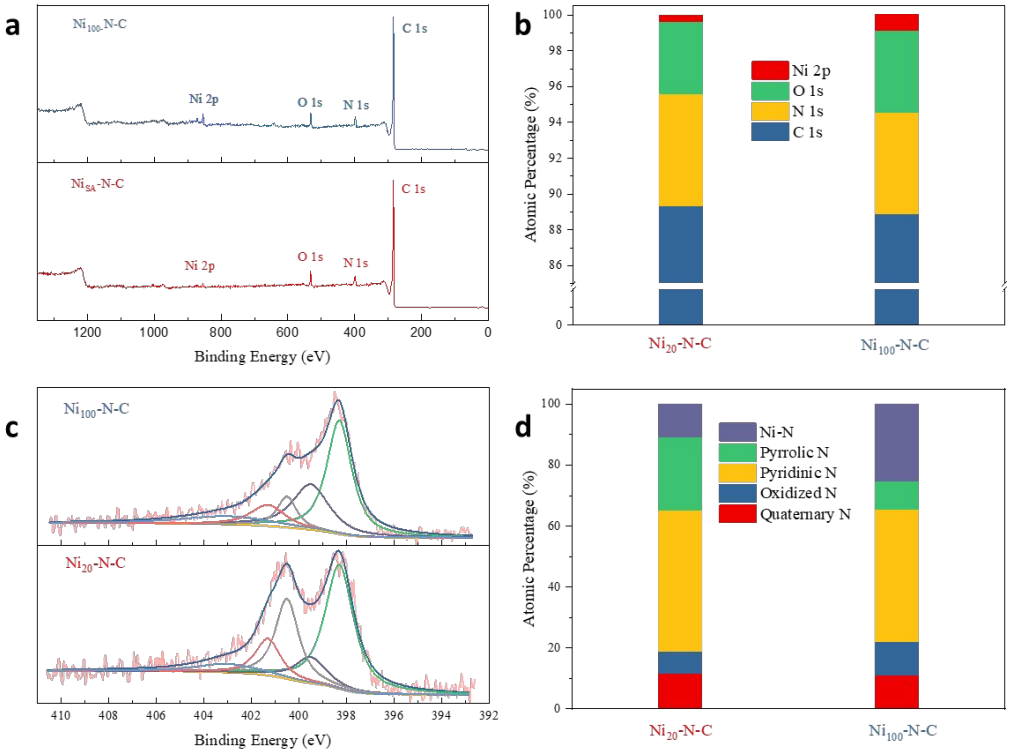

Figure S13. XPS survey spectra (a) and atomic content (b) of Ni_{20}-N-C and Ni_{100}-N-C, obtained by XPS measurements. (c) High-resolution XPS spectra of N 1s deconvoluted into five Voigt-type line-shaped peaks using the Shirley background. (d) Atomic content of five different kinds of N in Ni_{20}-N-C and Ni_{100}-N-C.

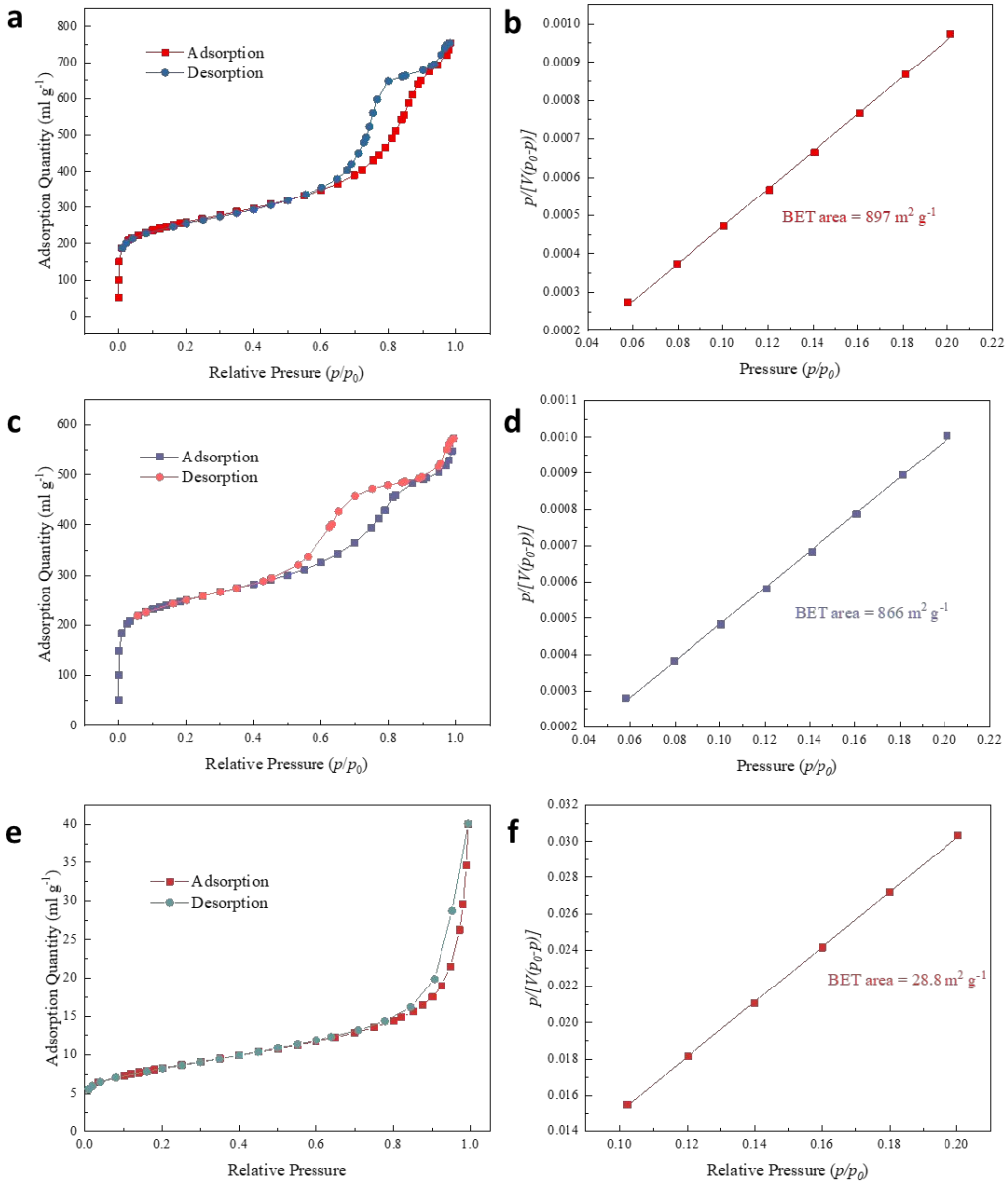

Figure S14. N_2 adsorption isotherms at 77 K and the BET surface area analysis of Ni_{20}-N-C (a, b), Ni_{100}-N-C (c, d) and Ni-AB (e, f).

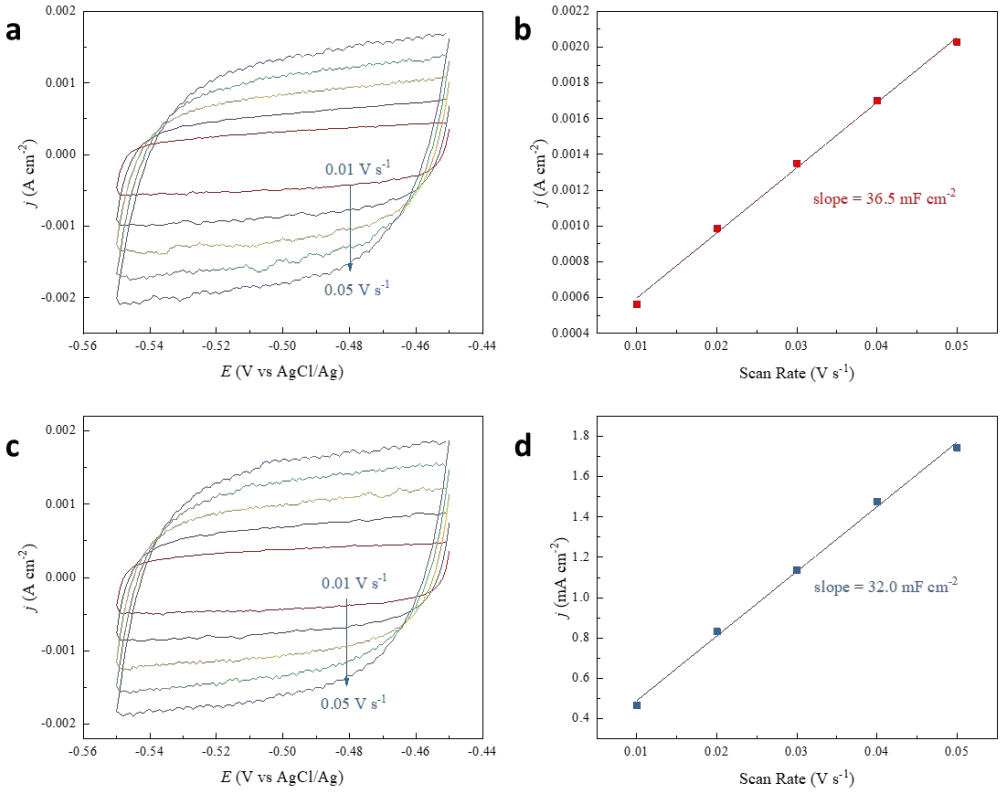

Figure S15. ECSA measurements and double-layer capacitance of Ni_{20}-N-C (a, b) and Ni_{100}-N-C (c, d).

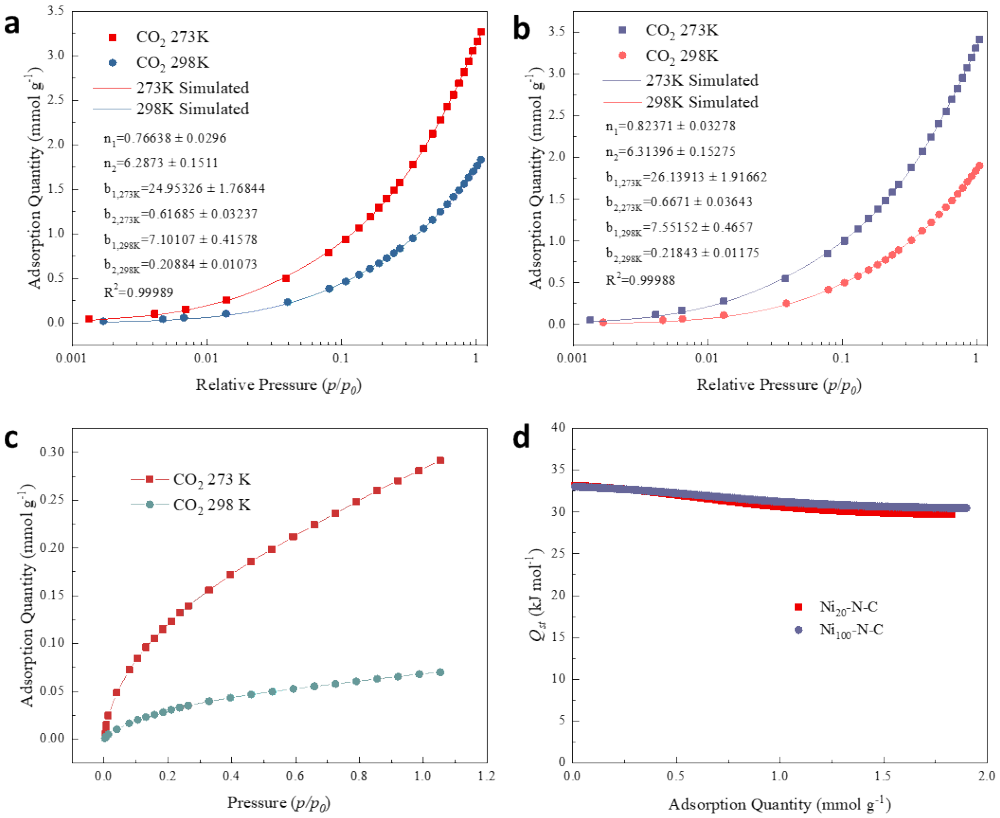

Figure S16. CO_2 adsorption simulates parameters for Ni_{20}-N-C (a), Ni_{100}-N-C (b) and CO_2 adsorption isotherms of Ni-AB at 273 and 298 K (c). (d) Isosteric heat of CO_2 adsorption for Ni_{20}-N-C and Ni_{100}-N-C.

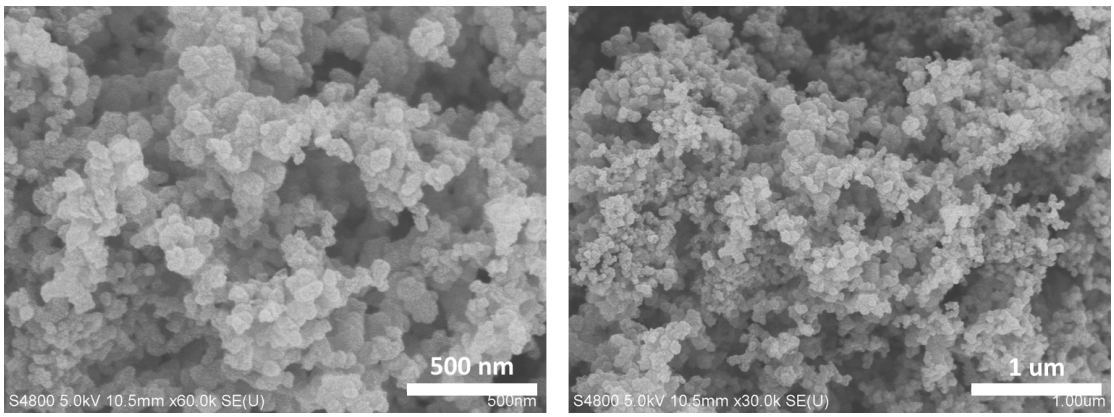

Figure S17. SEM images of Ni-AB.

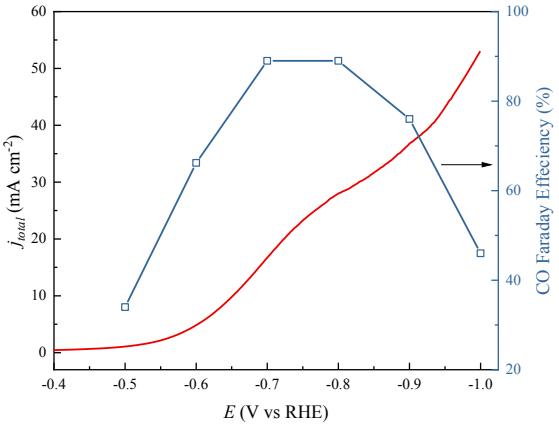

Figure S18. LSV curve and FE_{CO} for Ni-AB in 0.5 M $KHCO_3$ in an H-cell.

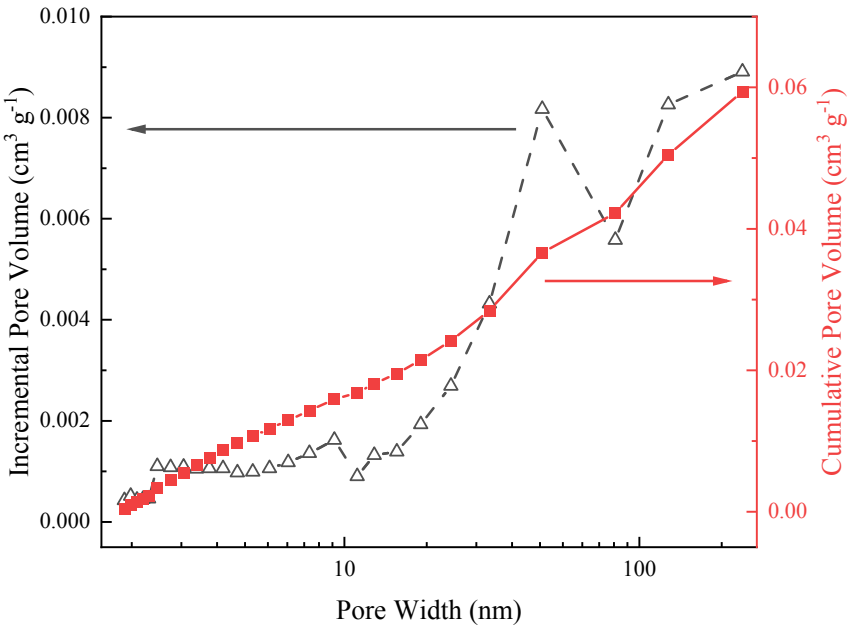

Figure S19. BJH pore distribution of Ni-AB catalyst.

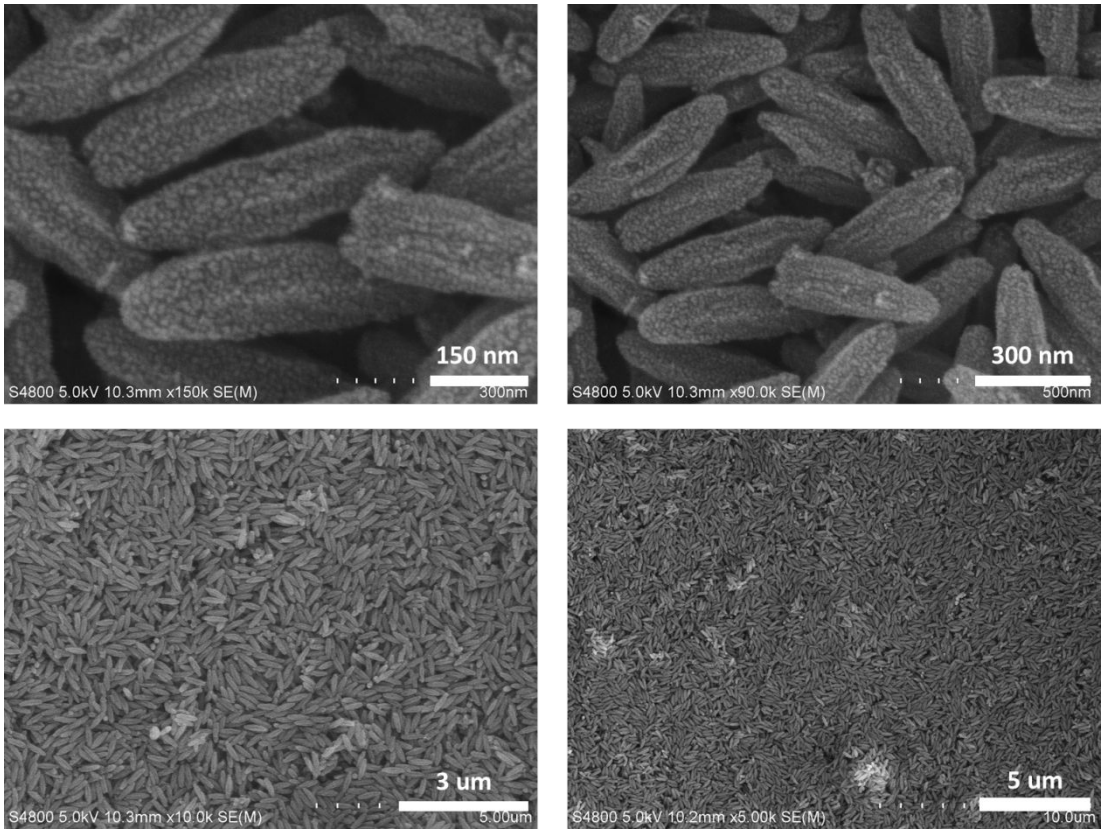

Figure S20. SEM images of Ni_{20}-N-C coated GDE.

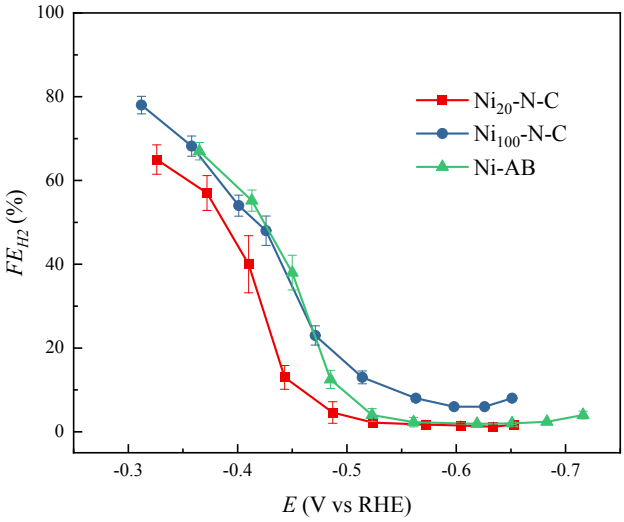

Figure S21. FE_{H2}s of Ni_{20}-N-C, Ni_{100}-N-C, and Ni-AB as a function of applied cathode potential in GDE with 2 M $KHCO_3$ as the electrolyte.

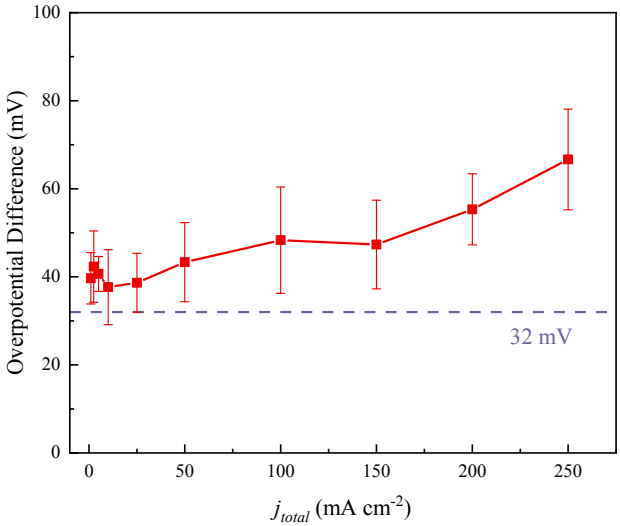

Figure S22. Overpotential differences between Ni-AB and Ni_{20}-N-C as a function of total current density. The purple line indicates the potential difference caused by CO_2 adsorption quantities of two catalysts.

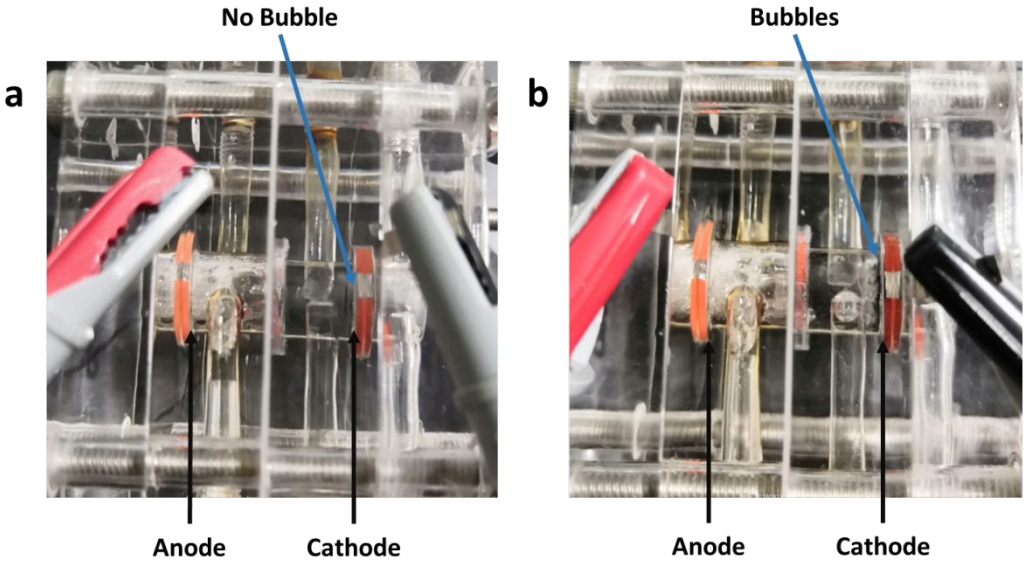

Figure S23. Photo of the electrolyzers under 250 mA cm^{-2} current density operation with Ni_{20}-N-C (a) and Ni-AB (b) coated cathodes.

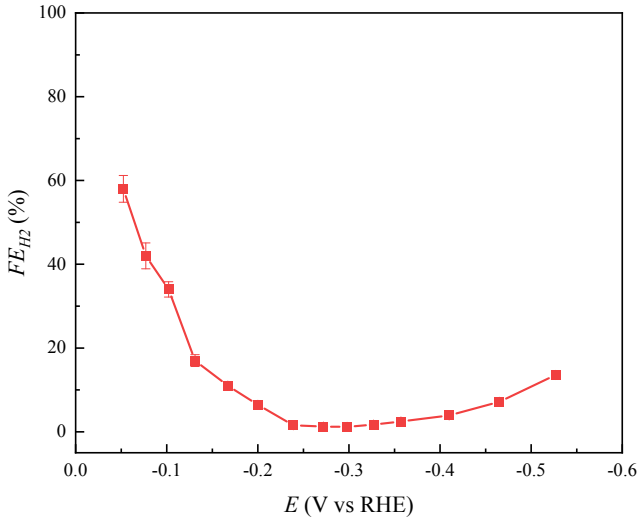

Figure S24. FE_{H2}s of Ni_{20}-N-C as a function of applied cathode potential in GDE configuration with 6 M KOH electrolyte.

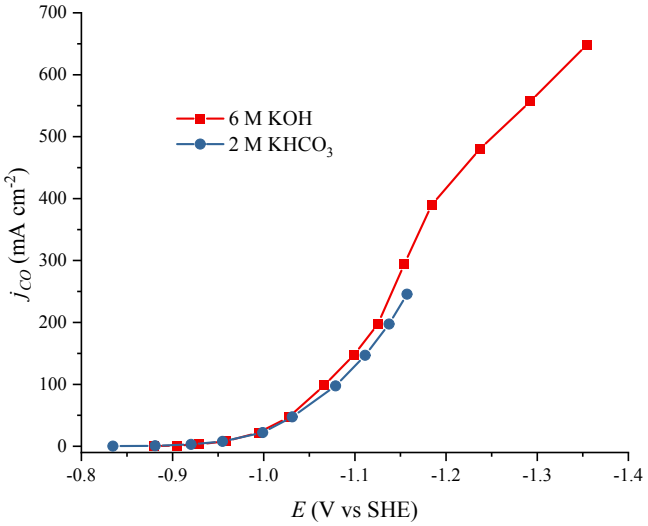

Figure S25. j_{co}-E curves of Ni_{20}-N-C in 2 M $KHCO_3$ and 6 M KOH utilizing SHE as reference.

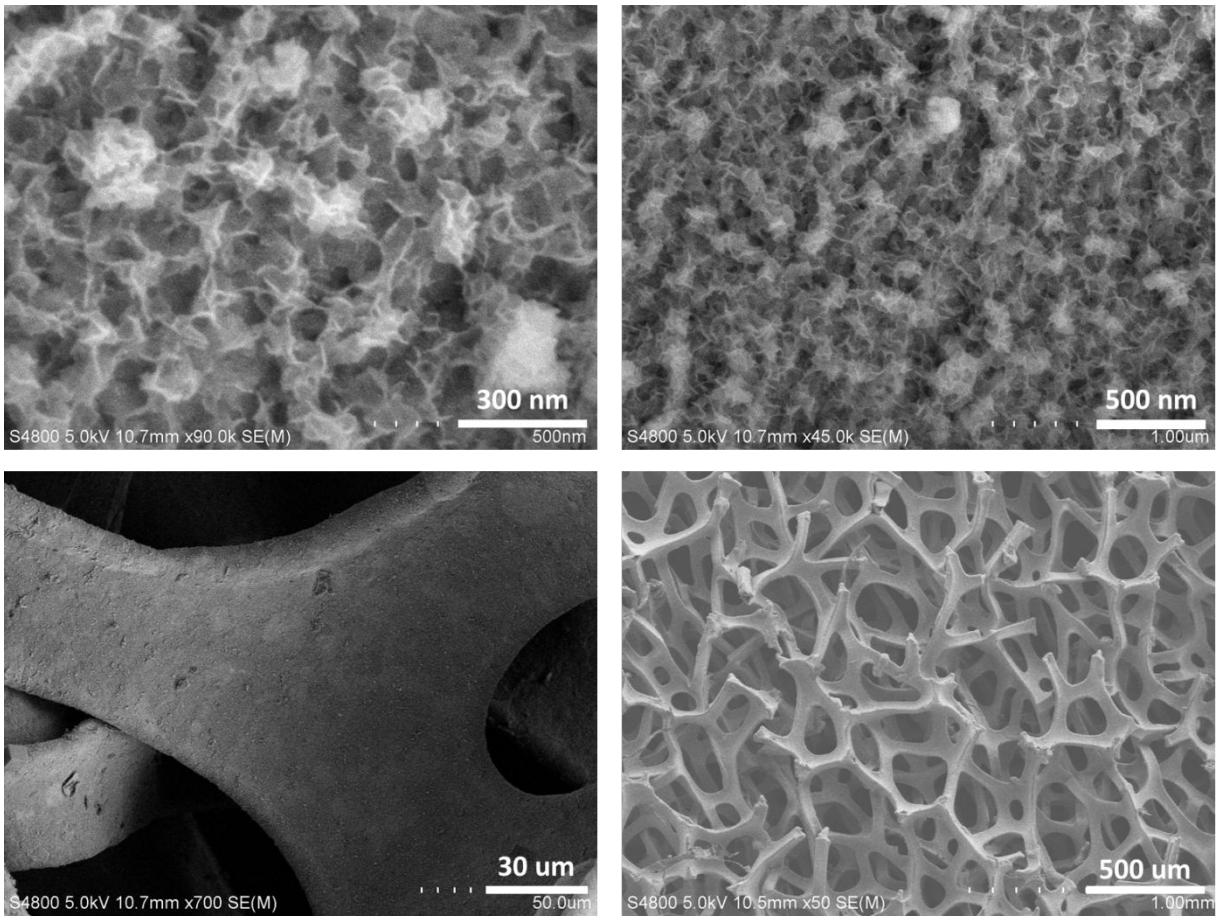

Figure S26. SEM images of $NiFeO_x$ anode.

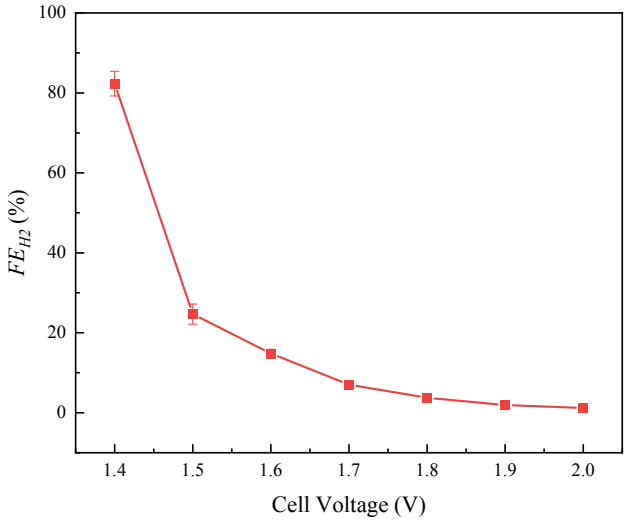

Figure S27. FE_{H2}s of Ni_{20}-N-C as a function of applied cathode potential in the full-cell test.

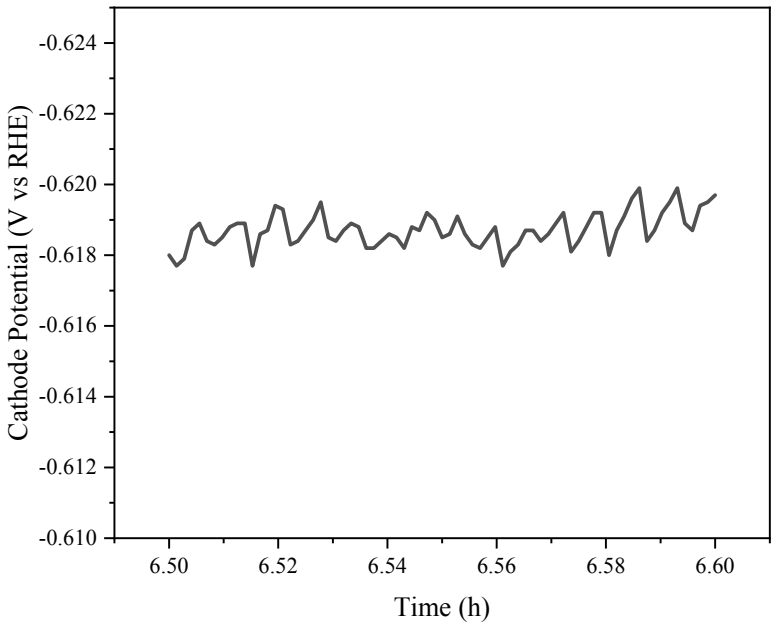

Figure S28. The influence of perspiration drops on the operating cathode potential.

Table S2 Gibbs free energies (G) calculation at 298 K and 1 atm

	E_{DFT} (eV)	E_{ZPE} (eV)	$\int_0^{298} C_V dT$ (eV)	$-T\Delta S$ (eV)	G(eV)
H_2	-6.769	0.265	-	-0.280	-6.784
CO_2	-22.956	0.268	-	-0.724	-23.412
CO	-14.778	0.132	-	-0.614	-15.260
H_2O†	-14.223	0.567	-	-0.566	-14.222
Ni-N-C	-646.624	-	-	-	-646.624
*COOH	-671.671	0.623	0.105	-0.214	-671.157
*CO	-661.427	0.148	0.060	-0.137	-661.279
*H	-648.526	0.168	0.012	-0.017	-648.363
Ni (100)	-159.331	-	-	-	-159.331
*COOH	-186.636	0.595	0.092	- 0.158	-186.106
*CO	-176.226	0.171	0.073	-0.134	-176.116
*H	-163.311	0.032	0.050	-0.094	-163.324

† H_2O was calculated under 0.035 atm.

Table S3 Catalysis performance comparison with reported systems

Catalyst	*Electrocell*	*Electrolyte*	*Onset potential (V vs RHE)*	*Overpotential (V)*	*Current density (mA cm^{-2})*	*Faradaic Efficiency (%)*	*TOF$_{mass}$ (s^{-1})*	*TOF$_{ECSA}$ (s^{-1})*	*Ref*
Ni$_{20}$-N-C	GDE	2 M $KHCO_3$	-0.29	0.54	250	98.8	8.9	60	
Ni$_{20}$-N-C	GDE	6 M KOH	0.03	0.163	200	98.7	7.1	48	This Work
Ni$_{20}$-N-C	GDE	6 M KOH	0.03	0.417	750	86	23	159	
Ni-NCB	MEA	0.1 M $KHCO_3$	~	~	73.8	99	6.36	~	*Joule* **3**, 265 (2019)[1]
WSe_2 NFs	RDE in H-cell	50 vol% EMIM-BF_4 solution	-0.164	0.654	330	~87	~	17	*Science* **353**, 467 (2016)[2]
Au needles	H-cell	0.5 M $KHCO_3$	-0.18	0.24	15	95	0.04	~	*Nature* **537**, 382 (2016)[3]
COF-367-Co	H-cell	0.5 M $KHCO_3$	~	0.56	~	77	0.046	0.53	*Science* **349**, 1208 (2015)[4]
A-Ni-NSG	H-cell	0.5 M $KHCO_3$	-0.18	0.61	23	97	4.11	~	*Nat. Energy* **3**, 140 (2018)[5]
Ni-NG	H-cell	0.5 M $KHCO_3$	-0.31	0.62	5.9	95	11.9	17	*Energy Environ. Sci.* **11**, 893 (2018)[6]
C-Zn_1Ni_4	H-cell	1 M $KHCO_3$	~	0.92	71.5	92	2.8	~	*Energy Environ. Sci.* **11**, 1204 (2018)[7]
[Co(qpy)]$^{2+}$@MWCNTs	H-cell	0.5 M $NaHCO_3$	~	0.47	19.9	99	12	~	*Angew. Chem. Int. Ed.* **57**, 7769 (2018)[8]
Ag NPs	GDE	7 atm 7 M KOH	-0.117	0.30	300	~99	~	~	*Energy Environ. Sci.* **11**, 2531 (2018)[9]
Ni-N-C	GDE	1 M $KHCO_3$	~	0.79	200	~90	~	~	*Energy Environ. Sci.*

Ag NPs	GDE	18 mol% EMIM-BF_4 solution	-0.28	~	~	96	6	~	**12**, 640 (2019)[10] *Science* **334**, 643 (2011)[11]
Ag NPs/MWCNTs	GDE	1 M KOH	~	0.66	350	95	~	~	*J. Mater. Chem. A.* **4**, 8573 (2016)[12]
CD-Ag/PTFE	GDE	1 M KOH	~	0.59	200	90	~	~	*ACS Energy Lett.* **3**, 2835 (2018)[13]
MWNT/PyPBI/Au	GDE	2 M KOH	-0.04	0.40	186	85	~	~	*ACS Energy Lett.* **3**, 193 (2018)[14]

References

1. Zheng, T. T.; Jiang, K.; Ta, N.; Hu, Y. F.; Zeng, J.; Liu, J. Y.; Wang, H. T., Large-Scale and Highly Selective CO_2 Electrocatalytic Reduction on Nickel Single-Atom Catalyst. *Joule* **2019,** *3* (1), 265-278.

2. Asadi, M.; Kim, K.; Liu, C.; Addepalli, A. V.; Abbasi, P.; Yasaei, P.; Phillips, P.; Behranginia, A.; Cerrato, J. M.; Haasch, R.; Zapol, P.; Kumar, B.; Klie, R. F.; Abiade, J.; Curtiss, L. A.; Salehi-Khojin, A., Nanostructured Transition Metal Dichalcogenide Electrocatalysts for CO_2 Reduction in Ionic Liquid. *Science* **2016,** *353* (6298), 467-470.

3. Liu, M.; Pang, Y.; Zhang, B.; De Luna, P.; Voznyy, O.; Xu, J.; Zheng, X.; Dinh, C. T.; Fan, F.; Cao, C.; de Arquer, F. P.; Safaei, T. S.; Mepham, A.; Klinkova, A.; Kumacheva, E.; Filleter, T.; Sinton, D.; Kelley, S. O.; Sargent, E. H., Enhanced Electrocatalytic CO_2 Reduction Via Field-Induced Reagent Concentration. *Nature* **2016,** *537* (7620), 382-386.

4. Lin, S.; Diercks, C. S.; Zhang, Y. B.; Kornienko, N.; Nichols, E. M.; Zhao, Y.; Paris, A. R.; Kim, D.; Yang, P.; Yaghi, O. M.; Chang, C. J., Covalent Organic Frameworks Comprising Cobalt Porphyrins for Catalytic CO_2 Reduction in Water. *Science* **2015,** *349* (6253), 1208-13.

5. Yang, H. B.; Hung, S. F.; Liu, S.; Yuan, K. D.; Miao, S.; Zhang, L. P.; Huang, X.; Wang, H. Y.; Cai, W. Z.; Chen, R.; Gao, J. J.; Yang, X. F.; Chen, W.; Huang, Y. Q.; Chen, H. M.; Li, C. M.; Zhang, T.; Liu, B., Atomically Dispersed Ni(I) as the Active Site for Electrochemical CO_2 Reduction. *Nat. Energy* **2018,** *3* (2), 140-147.

6. Jiang, K.; Siahrostami, S.; Zheng, T. T.; Hu, Y. F.; Hwang, S.; Stavitski, E.; Peng, Y. D.; Dynes, J.; Gangisetty, M.; Su, D.; Attenkofer, K.; Wang, H., Isolated Ni Single Atoms in Graphene Nanosheets for High-Performance CO_2 Reduction. *Energy Environ. Sci.* **2018,** *11* (4), 893-903.

7. Yan, C.; Li, H.; Ye, Y.; Wu, H.; Cai, F.; Si, R.; Xiao, J.; Miao, S.; Xie, S.; Yang, F.; Li, Y.; Wang, G.; Bao, X., Coordinatively Unsaturated Nickel–Nitrogen Sites Towards Selective and High-Rate CO_2 Electroreduction. *Energy Environ. Sci.* **2018,** *11* (5), 1204-1210.

8. Wang, M.; Chen, L.; Lau, T. C.; Robert, M., A Hybrid Co Quaterpyridine Complex/Carbon Nanotube Catalytic Material for CO_2 Reduction in Water. *Angew. Chem. Int. Ed.* **2018,** *57* (26), 7769-7773.

9. Gabardo, C. M.; Seifitokaldani, A.; Edwards, J. P.; Dinh, C. T.; Burdyny, T.; Kibria, M. G.; O'Brien, C. P.; Sargent, E. H.; Sinton, D., Combined High Alkalinity and Pressurization Enable Efficient CO_2 Electroreduction to CO. *Energy Environ. Sci.* **2018,** *11* (9), 2531-2539.

10. Möller, T.; Ju, W.; Bagger, A.; Wang, X.; Luo, F.; Ngo Thanh, T.; Varela, A. S.; Rossmeisl, J.; Strasser, P., Efficient CO_2 to CO Electrolysis on Solid Ni–N–C Catalysts at Industrial Current Densities. *Energy Environ. Sci.* **2019,** *12* (2), 640-647.

11. Rosen, B. A.; Salehi-Khojin, A.; Thorson, M. R.; Zhu, W.; Whipple, D. T.; Kenis, P. J.; Masel, R. I., Ionic Liquid-Mediated Selective Conversion of CO_2 to CO at Low Overpotentials. *Science* **2011,** *334* (6056), 643-644.

12. Ma, S. C.; Luo, R.; Gold, J. I.; Yu, A. Z.; Kim, B.; Kenis, P. J. A., Carbon Nanotube Containing Ag Catalyst Layers for Efficient and Selective Reduction of Carbon Dioxide. *J. Mater. Chem. A* **2016,** *4* (22), 8573-8578.

13. Dinh, C. T.; de Arquer, F. P. G.; Sinton, D.; Sargent, E. H., High Rate, Selective, and Stable Electroreduction of CO_2 to CO in Basic and Neutral Media. *ACS Energy Lett.* **2018,** *3* (11), 2835-2840.

14. Verma, S.; Hamasaki, Y.; Kim, C.; Huang, W. X.; Lu, S.; Jhong, H. R. M.; Gewirth, A. A.; Fujigaya, T.; Nakashima, N.; Kenis, P. J. A., Insights into the Low Overpotential Electroreduction of CO_2 to CO on a Supported Gold Catalyst in an Alkaline Flow Electrolyzer. *ACS Energy Lett.* **2018,** *3* (1), 193-198.